Title

Geomorphological analysis of the southwestern margin of Xanadu, Titan: Insights on tectonics

Authors

Pietro Matteoni[1], Giuseppe Mitri[1,2], Valerio Poggiali[3], Marco Mastrogiuseppe[4]

[1]International Research School of Planetary Sciences, Università d'Annunzio, Pescara, Italy

[2]Dipartimento di Ingegneria e Geologia, Università d'Annunzio, Pescara, Italy

[3]Department of Astronomy, Cornell University, Ithaca, NY, USA

[4]Dipartimento di Ingegneria dell'Informazione, Elettronica e Telecomunicazioni (DIET), Sapienza Università di Roma, Rome, Italy

Corresponding author: Pietro Matteoni (pietro.matteoni@unich.it)

Key Points

- We conducted a geomorphological mapping of southwestern Xanadu, based on radar data
- Newly available topographic data were used
- Southwestern Xanadu is interpreted as a pull-apart basin formed by trans-tensional tectonic activity

Abstract

Evidence for tectonic activity on Titan is shown by the presence of eroded mountain ranges, although it is unclear whether their origin is endogenic. Xanadu is an equatorial region characterized by an articulated topography, even though overall it has a lower average elevation compared to its surroundings. We investigated Xanadu's southwestern margin, a part of the region which is comprised of heavily eroded and rugged terrains to the North and East and of smoother, more uniform terrains to the West and South. An extensive fluvial network characterizes its central portions. Through detailed geomorphological mapping on Synthetic Aperture Radar (SAR) data and analysis of both fluvial drainage patterns and Digital Terrain Models (DTMs), we identified several putative tectonic structures in this area. We propose that central southwestern Xanadu is a pull-apart basin formed by trans-tensional tectonics, bordered by both normal and thrust faults. Such basin is characterized by strike-slip faulting within it, on which a now inactive fluvial network is subsequently imposed.

Plain Language Summary

Saturn's largest moon, Titan, shows several mountain ranges on its surface. It is unclear whether they are formed just by the action of the erosive agents or some bigger scale processes related to Titan's interior are involved. Xanadu is an equatorial region characterized by an articulated topography, even though its surrounding regions stand higher. We investigated Xanadu's southwestern margin, which is characterized by many different terrain types and by the presence of a hydrocarbon-related fluvial system. At Titan's surface conditions of pressure and temperature, hydrocarbons are in liquid state and can therefore form rivers. Using radar data from the Cassini mission, we mapped the differences in morphology of each terrain in the region. Combining these results with those derived from analysis of sparsely available Cassini's elevation data, we identified several areas that may testify the influence of Titan's internal processes on shaping the region.

1. Introduction

Saturn's largest moon, Titan, is currently identified as the only extra-terrestrial body whose surface supports standing liquid bodies. It is also considered, along with Earth and early Mars, as one of the three Solar System bodies to have had an active hydrologic cycle (A. G. Hayes, 2016; A. G. Hayes et al., 2018; E. R. Stofan et al., 2007). Furthermore, Titan's atmosphere is the second densest amongst the terrestrial planets and icy satellites. Present day surface–atmosphere interactions make aeolian, fluvial, pluvial and lacustrine processes prominent on a scale seen only on Earth (R. M. C. Lopes et al., 2010). The satellite's atmosphere consists mainly of nitrogen (N_2 ~97%), methane (CH_4 ~1.4% in the troposphere, 5% at the surface) and hydrogen (H_2 ~0.2%) with traces of more complex hydrocarbons, nitriles, oxygen compounds and argon as analyzed by the Huygens probe (A. Coustenis et al., 2010; Athena Coustenis, 2005; Dalton et al., 2010). Under Titan's surface conditions (pressure ~1.5 bars; temperature ~91–95 K), methane (CH_4) and ethane (C_2H_6) are both able to condense out of the atmosphere and precipitate to the surface, where the fluid runoff concentrates, incises channels and transports sediment (Birch et al., 2017; A. G. Hayes et al., 2018).

Moreover, landforms similar to those common on Earth are found on Titan, including lakes and seas (A. Hayes et al., 2008; Mastrogiuseppe et al., 2018; Mitri et al., 2007, 2019; E. R. Stofan et al., 2007) dunes fields up to hundreds of meters in height (Malaska, Lopes, Hayes, et al., 2016; Mastrogiuseppe et al., 2014; J. Radebaugh et al., 2008), impact craters (Elachi et al., 2006; E. R. Stofan et al., 2006; Wood et al., 2010), fluvial channels and valleys (Burr et al., 2009; Le Gall et al., 2010; Lorenz et al., 2008), fans and deltas (Witek and Czechowski, 2015; Birch et al., 2016; Radebaugh et al., 2016) and mountains (Barnes et al., 2007; Cook-Hallett et al., 2015; Liu, Radebaugh, Harris, Christiansen, Neish, et al., 2016; Mitri et al., 2010; Jani Radebaugh et al., 2007). Such characteristics make Titan an ideal laboratory to study and compare terrestrial and planetary landscape-shaping processes (A. G. Hayes, 2016), although its landforms have all been formed and developed under very different environmental and physical conditions in comparison to Earth (Birch et al., 2017).

A consensus is shared on the presence of a subsurface ocean on Titan (Iess et al., 2012; Lunine, 2017; Mitri et al., 2010, 2014; Nimmo, 2018; Stern et al., 2018). Due to its orbital eccentricity value (e = 0.028) Titan is subject to a large variability of tidal forces intensities along its 16-day orbit around Saturn (Iess et al., 2012). Analysis of its response to the varying external gravity field has demonstrated the presence of a global subsurface ocean, likely lying above high-pressure ices (ice V, VI), which decouples an ice I shell (supposed to have a thickness of 70-100 km) from the deeper interior (Mitri et al., 2010, 2014). Such ocean should have a high salinity, as a result of its inferred relatively high density (Mitri et al., 2014), which was in turn derived from the measured tidal Love number, $k_2 = 0.589 \pm 0.150$ (Iess et al., 2012). Tidal heating does not play a big role on Titan, since it is not in orbital resonance with other satellites; therefore, the primary thermal energy source should be a progressively decreasing heat flux, due to radiogenic decay. This preserves the existence of the ocean through geological time but results in gradual global cooling (Mitri et al., 2010; Tobie et al., 2006). Density differences among the various water and ice phases generate the thickening of the ice layers (above and beneath the liquid layer) and the progressive freezing of the ocean. Concurrently, its assumed high salinity should inhibit further refreezing. Ultimately, a global radial contraction through volume decrease occurs (Mitri et al., 2010). The surficial expressions of such a compressive stress field would be long-wavelength folds and fold-and-thrust belts (Mitri et al., 2010). This model best explains the observed high elevation ridges (e.g., Solomonidou et al., 2013; Liu et al., 2016a,b). Still, it does not completely fit with the ridges' general orientation - E-W around the Equator and N-S at high latitudes - which have been related to polar thinning of the outer ice shell (Cook-Hallett et al., 2015).

Therefore, evidence for tectonic activity on Titan is exemplified by the presence of eroded mountain ranges (Mitri et al., 2010; Jani Radebaugh et al., 2007), although it is unclear whether their origin is endogenic (Moore & Pappalardo, 2011). Due to poor Synthetic Aperture Radar (SAR) resolution and paucity of low error range elevation data (i.e. Cassini's Radio Detection And Ranging Instrument – RADAR – altimetry) tectonic indicators on Titan might be identified by

indirect approaches such as analysis of drainage networks' azimuths (Burr et al., 2009; Burr, Drummond, et al., 2013) and planform geometries (e.g. width function, channel sinuosity) (Black et al., 2012).

Xanadu is an equatorial region, extending for an area of about 4000 × 2500 km. It was first observed using the Hubble Space Telescope. It is the brightest (at all wavelengths) and largest geologic feature on Titan's surface. It is located on Titan's leading hemisphere and it interrupts the sand seas, which otherwise dominate the equatorial regions (R. M. C. Lopes, Wall, et al., 2019). It has a generally high SAR-brightness indicating that it is made up of rugged terrains (J. Radebaugh et al., 2011). Xanadu's characteristics make it unique among Titan's regions and indicate a long and complex geological history: deeply eroded, incised, mountain ranges are carved by extensive fluvial networks emptying in fans to the south; linear features likely tectonic in nature are widespread, as well as impact craters which are twice as common compared to the rest of Titan (Birch et al., 2016; Burr et al., 2009; Le Gall et al., 2010; J. Radebaugh et al., 2011; Wood et al., 2010). Despite the wide distribution of mountains and high local topographic variations, overall the region has a lower average elevation compared to its surroundings (R. M. C. Lopes, Wall, et al., 2019; J. Radebaugh et al., 2011) as evident from RADAR altimetry data, SARTopo data, shape and topographic models, and Digital Terrain Models (DTMs) (Corlies et al., 2017; Kirk et al., 2012; Lorenz et al., 2013; Mitri et al., 2014; Stiles et al., 2009; Zebker et al., 2009). This represents Xanadu's most intriguing characteristic and brought several authors to study this region; yet, the origins of Xanadu remain enigmatic. Brown et al. (2011) suggested that the geomorphology of Xanadu is consistent with the site of an ancient impact, while Langhans et al. (2013) proposed that it is a remnant of past tectonic activity, reworked and resurfaced in recent times by fluvial processes. A detailed study of the Xanadu region, which further divides it into several units, is presented in Radebaugh et al. (2011). In contrast to Brown et al. (2011), these authors proposed that Xanadu has had a complex tectonic history, involving both compressional and extensional events. In a first tectonic phase, the region would have undergone crustal thickening via N-S directed regional scale compression. This phase

would have had surface expressions such as oriented parallel mountain ridges (and related valleys) and fold-and-thrust belts. Subsequently an extensional event would have occurred, favored by slip along region-bounding faults, resulting in horst-and-graben-like structures. The extended fluvial network in southwestern Xanadu is argued (Burr et al., 2009; Burr, Drummond, et al., 2013) to have developed over a pre-existing E-W tectonic fabric (rectangular-type pattern), with a general draining direction from N to S. The tectonic style responsible for generating such a pattern is thought to be extensional, by analogy with terrestrial examples.

Previous geomorphologic works of Titan include global mappings (R. M. C. Lopes, Malaska, et al., 2019; R. M. C. Lopes et al., 2010; Rosaly M.C. Lopes et al., 2016) and several regional ones (Birch et al., 2017; Malaska, Lopes, Williams, et al., 2016; Moore et al., 2014; J. Radebaugh et al., 2011; Williams et al., 2011). The present study aims at investigating southwestern Xanadu's formation and the related geological processes, through detailed geomorphological mapping together with both qualitative and quantitative analysis of drainage patterns and DTMs.

2. Methods

A geomorphological map of SW Xanadu was produced (Figure 1) based on Cassini's SAR images (spatial resolution: ~350 m to 1.5 km; Elachi et al., 2005), which were imported in various Geographical Information System (GIS) environments along with topographic data in the form of RADAR altimetry (vertical error range: ± 30 m; Zebker et al., 2009), SARTopo (± 150 m; Stiles et al., 2009) and DTMs processed through stereophotogrammetry (± 100 m; Kirk et al., 2012). DTMs are available only in sparsely distributed areas of SAR swaths overlap. All datasets have been projected using the same reference system (equidistant cylindrical projection) centered at 0°N, 0°E.

The interpretation of surface geomorphology has been the main technique used to characterize the hypothesized surficial expressions of Titan's tectonism. Distinction among different geomorphological units has been conducted manually and is based on: SAR backscatter

characteristics, units' texture, their general appearance and geomorphology (Williams et al., 2011). Where available, topographic data (SARTopo and DTMs) have been used to further constrain the geomorphological interpretation. In compliance with the guidelines given by Ford et al. (1993), Elachi et al. (2005) and Stofan et al. (2008), Titan's SAR dataset has been interpreted considering that SAR's backscatter coefficient σ^0 (classified as "high", "medium", "low" or "variable"; values range in linear scale: $0 \leq \sigma^0 \leq \sim 1.5$) depends on: local incidence angle, surface roughness, volume scattering and dielectric properties (Cook-Hallett et al., 2015; Elachi et al., 2005; Ford et al., 1993; R. M. C. Lopes et al., 2010; Malaska, Lopes, Williams, et al., 2016; Williams et al., 2011). Along with geomorphological units, a network of linear features interpreted as fluvial valleys (Section 3.1.8) have been identified and their azimuths are investigated via rose diagrams analysis (Figure 2a). Furthermore, several linear structures interpreted as strike-slip faults (Section 3.2.1) have been analyzed via rose diagrams (Figure 2b).

3. Results

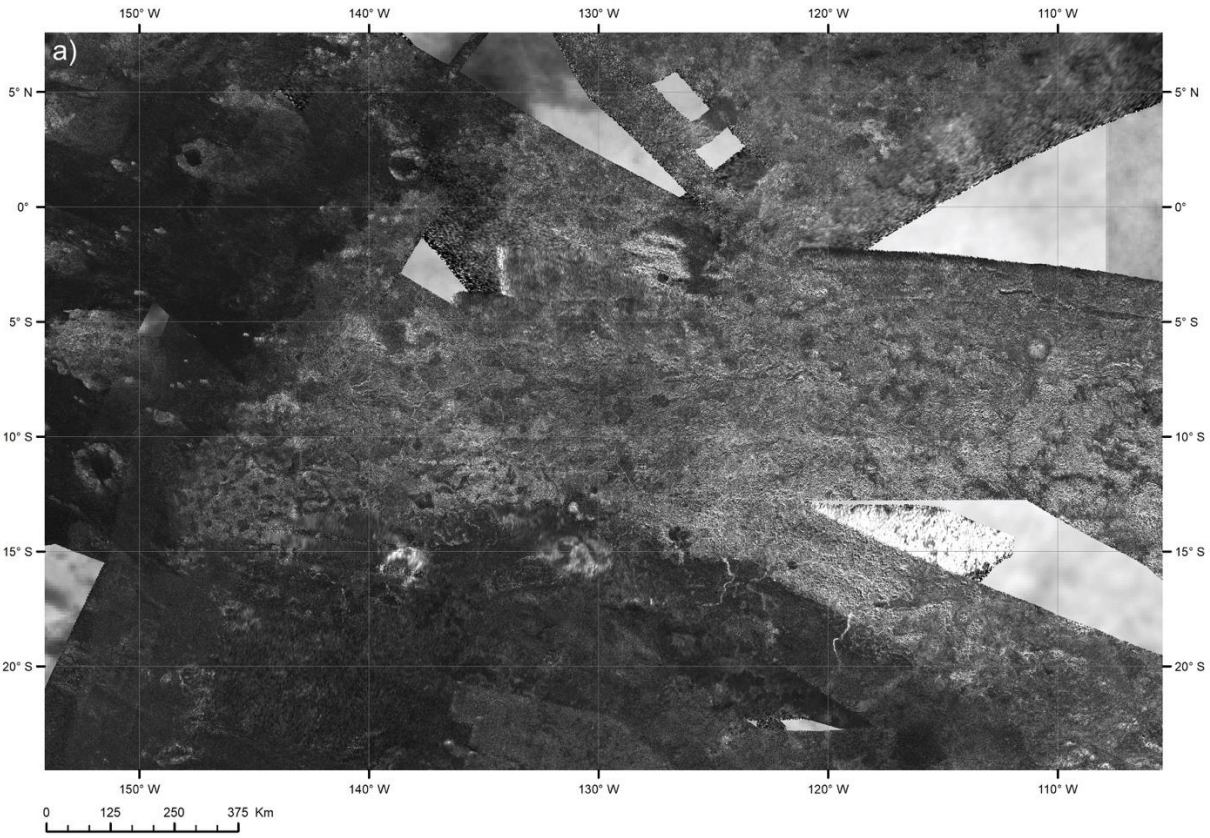
a)
150° W
140° W
130° W
120° W
110° W
5° N
0°
5° S
10° S
15° S
20° S
0
125
250
375 Km

179

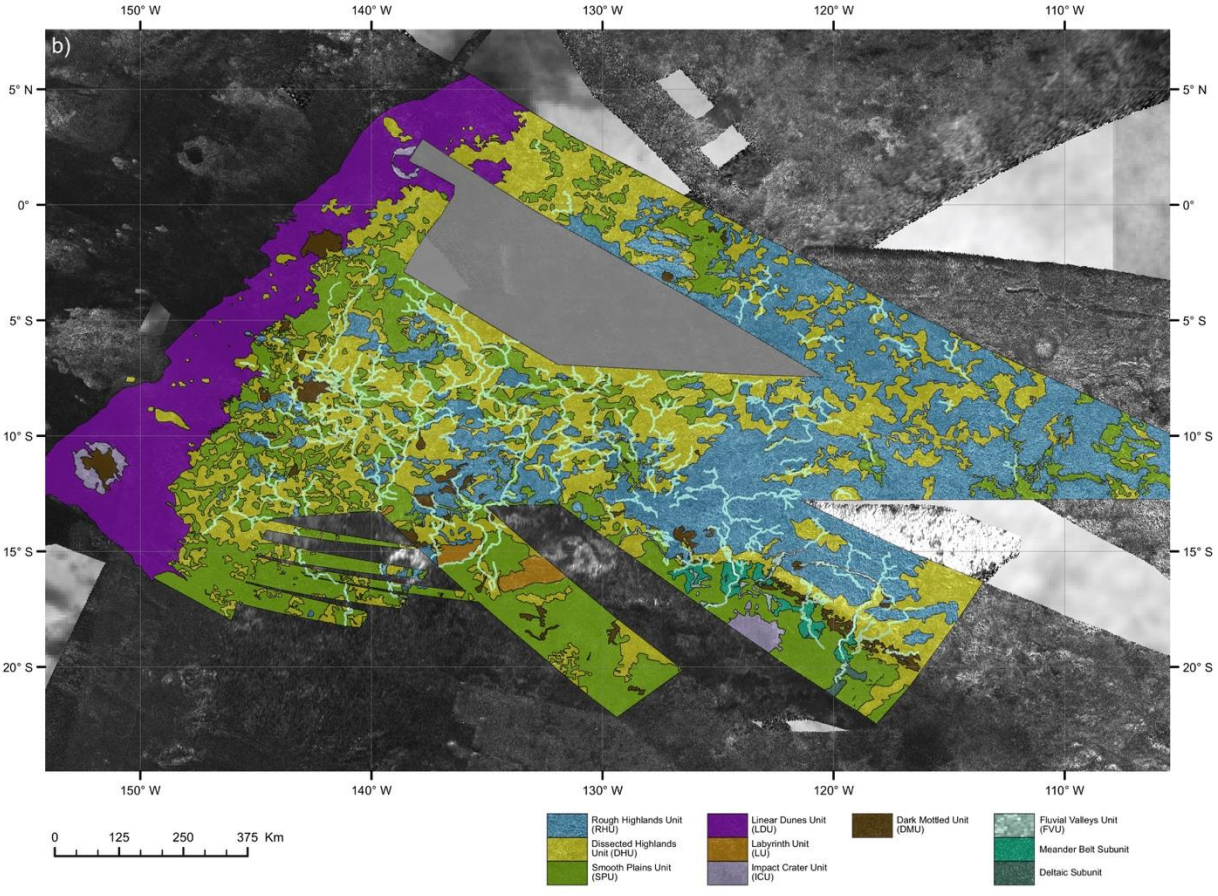
b)
150° W
140° W
130° W
120° W
110° W
5° N
0°
5° S
10° S
15° S
20° S
0
125
250
375 Km
Rough Highlands Unit (RHU)
Dissected Highlands Unit (DHU)
Smooth Plains Unit (SPU)
Linear Dunes Unit (LDU)
Labyrinth Unit (LU)
Impact Crater Unit (ICU)
Dark Mottled Unit (DMU)
Fluvial Valleys Unit (FVU)
Meander Belt Subunit
Deltaic Subunit

180

Figure 1. a) SAR images mosaic of southwestern Xanadu. **b)** Geomorphological map of southwestern Xanadu, displaying the same area as in panel a. The units' legend is displayed in the bottom-right corner. North is up in both panels.

The main outcome of this study is a geomorphological map of southwestern Xanadu, shown in Figure 1b, based on Cassini's SAR images (Figure 1a). Hereafter follows a detailed definition, description and interpretation of the encountered geomorphological units.

3.1 Geomorphological Units Description and Interpretation

3.1.1 Rough Highlands Unit (RHU)

Rough Highlands Unit (RHU, marked in blue; Figure 1b and Sup. Figure 1b) is characterized by a generally high σ^0, yet with an observable diffused bright/dark pairing. It is comprised by linear ridges or irregular patches, always embayed by SAR-darker materials. In the mapped area it is the brightest unit, whereas its texture is intensely rugged and dissected (Sup. Figure 1a-b). The superimposition of elevation data on the SAR mosaic has shown that the RHU usually coincides with the highest topography. Similar observations on a global scale led to the interpretation that this unit consists of mountainous terrains composed of icy bedrock (Barnes et al., 2007; Jani Radebaugh et al., 2007). The high σ^0 most probably depends on a high surface roughness given by granulometric differences, while the bright/dark pairing SAR appearance may be due to different orientations of the slopes (Cook-Hallett et al., 2015).

The overall morphology of this unit is distinctive of ridges eroded by the exogenous agents, whose action results in the typical rugged and dissected, crenulated SAR texture (Jani Radebaugh et al., 2007). Considering the unambiguous theoretical and observational constraints, similar interpretations have been given by previous geomorphological studies on different Titan's regions

206 (Birch et al., 2017; R. M. C. Lopes et al., 2010; Malaska, Lopes, Williams, et al., 2016; Williams et
207 al., 2011).
208
209 **3.1.2 Dissected Highlands Unit (DHU)**
210 Dissected Highlands Unit (DHU, marked in yellow; Figure 1b and Sup. Figure 1d) has variable σ^0,
211 ranging from medium-high to medium-low (Sup. Figure 1c). It is comprised of mottled and
212 dissected patches, usually surrounding the RHU through quite abrupt boundaries (Sup. Figure 1d).
213 The main discriminant between the two units is a relatively well distributed and homogenous
214 "grainy" texture of the DHU. The analysis of topographic data has shown how the DHU elevation is
215 variable but generally high compared to the other units, yet lower than the RHU.
216 The DHU is interpreted as the result of the erosional breakdown of mountainous terrains, mainly
217 by fluvial erosion and flank deposition (Aharonson et al., 2013; R. M. C. Lopes et al., 2010). These
218 processes produce SAR brightness variations (i.e., the "grainy" texture previously mentioned),
219 which are likely dominated by changes in surface roughness, volume scattering and compositional
220 variations.
221
222 **3.1.3 Smooth Plains Unit (SPU)**
223 Smooth Plains Unit (SPU, marked in green; Figure 1b and Sup. Figure 1f) is formed by deposits of
224 medium-low σ^0 material, with relatively homogenous appearance (Rosaly M.C. Lopes et al., 2016).
225 It tends to have gradational boundaries and occurs in patches that are generally hundreds of km in
226 extent (Sup. Figure 1e). It is a unit typical of topographically depressed areas, surrounded by the
227 RHU and DHU (Sup. Figure 1f). It is composed of SAR-dark materials, probably of organic origin,
228 resulting either from fluvial deposition or from the accumulation of photolysis products created in
229 the upper atmosphere (Aharonson et al., 2013; Rosaly M.C. Lopes et al., 2016). Morphologically,
230 the SPU comprises small basins and widespread plains, while most of the inferred fluvial valleys
231 are superimposed on it.

3.1.4 Linear Dunes Unit (LDU)

Linear Dunes Unit (LDU, marked in purple; Figure 1b and Sup. Figure 1h) is formed by parallel to subparallel low σ^0 lineations on a variable σ^0 substrate. SAR-bright lineations can sometimes be seen coincident with dark ones, along an E-W or SW-NE strike (Sup. Figure 1g). Where present, these features are superposed on all other units and embay inferred topographic barriers, diverting around these, or sometimes arresting at their contact. Tapering relative relationships are also locally observed (Sup. Figure 1h). Topography across the regions has shown that the LDU terrains are not flat as they have rises and falls, but outcrops of RHU and DHU are often locally higher. The coincident SAR-bright lines sometimes observed are consistent with specular reflections off a dune crest, when the incidence angle of the radar matches that of the dune crest. Williams et al. (2011) described this unit as longitudinal dunes composed of fine-grained fragmental material deposited by aeolian processes (see also Radebaugh et al., 2008).

3.1.5 Labyrinth Unit (LU)

Labyrinth Unit (LU, marked in orange; Figure 1b and Sup. Figure 2f) presents very dissected terrains, generally with medium σ^0 even though clear bright–dark pairing in the up range-down range side is evident (Sup. Figure 2e), which indicates uplands with canyons or valleys containing radar-dark floors or fill (Sup. Figure 2f).

This unit is interpreted (Malaska, Lopes, Williams, et al., 2016; Moore et al., 2014) as dissected plateaux (due to generally high elevations) or remnant ridges of eroded organic materials that then release such materials into the plains and downstream basins.

3.1.6 Impact Craters Unit (ICU)

As previously mentioned, Titan has some recognizable impact craters on its surface (Bottke & Norman, 2017; Neish et al., 2016; Wood et al., 2010). Such hypothesized craters can be discriminated from the adjacent units by their corona-like morphology, as high in σ^0 as the RHU, which surrounds a circular SAR-intermediate/dark area. We classified these morphologies as Impact Craters Unit (ICU, marked in pink; Figure 1b and Sup. Figure 2b). In one case (18°S; 123°W) two small patches are identified nearby, yet outside of the corona, and have been defined as related to the impact (Sup. Figure 2a)

The corona-like morphology is interpreted as an impact crater's outer rim (R. M. C. Lopes et al., 2010). What is surrounded by the rim is inferred to be filling material, a mixture of bedrock exposed by the impact and organics further emplaced by atmospheric airfall and aeolian processes (Malaska, Lopes, Williams, et al., 2016). The aforementioned two small patches are interpreted as crater ejecta, deposited as a consequence of the energetic impact event. All the above subunits have not been distinguished from each other using different identification colors, as it is not directly relevant to the main aim of this work and are thus joined in the ICU (Sup. Figure 2b).

3.1.7 Dark Mottled Unit (DMU)

Dark Mottled Unit (DMU, marked in brown; Figure 1b and Sup. Figure 2d) is the unit with the lowest local σ^0. It occurs in small irregular patches of lobate to mottled and angular morphologies (Sup. Figure 2c)

The DMU has been previously interpreted as low elevation localized basins dampened by liquid hydrocarbons or other damp materials, but do not contain deep lakes of liquid hydrocarbons as observed at the north pole (Mastrogiuseppe et al., 2019). Alternatively, these could contain finer grained materials or materials that have less organized structure (thus less backscatter) than the surrounding terrain (Malaska, Lopes, Williams, et al., 2016) (Sup. Figure 2d).

This hypothesis is confirmed by the superimposition of DTMs, with the unit's patches corresponding to local topographic lows all around the investigated area. It can be further observed

283 that the DMU is often found at the onset or end of fluvial units and may then represent local basins
284 and/or fluvial spring areas. In very rare cases this unit exhibits the typical fan morphology, in
285 proximity of inferred fluvial valleys. These isolated patches can then be examples of Titan's alluvial
286 fans (Birch et al., 2016; J. Radebaugh et al., 2016).
287
288 **3.1.8 Fluvial Valleys Unit (FVU)**
289 Fluvial Valleys Unit (FVU, marked in light blue; Figure 1b and Sup. Figure 2h) is characterized by
290 wide (~1-6 km), long (up to ~200-300 km), rough, sinuous, SAR-bright features; widths often vary
291 noticeably along-distance (Sup. Figure 2g). The wider ends terminate and are superposed on SAR-
292 dark terrain, mainly SPU, while the narrower ends reach SAR-bright terrain, usually RHU (Sup.
293 Figure 2h).
294 Considering the hydrocarbon cycle likely ongoing on Titan (Athena Coustenis, 2005; A. Hayes
295 et al., 2008; A. G. Hayes, 2016) some feature responsible for the surficial liquid's runoff must exist.
296 Furthermore, Huygens' DISR instrument imaged branched lineations and rounded cobbles around
297 the Huygens Landing Site (10.6°S; 191°W), the only location on Titan's surface where observations
298 are not questionable (Tomasko et al., 2005). These have been interpreted, respectively, as fluvial
299 valley networks with inset streams formed by flowing methane and as material transported by
300 flowing liquid. This hypothesis is mainly suggested by analogy with Earth's fluvial processes
301 (Tomasko et al., 2005). Orbital data (RADAR, VIMS, ISS) have also shown networked lineations,
302 distributed at different latitudes. These have been interpreted as fluvial channels, instead of valleys
303 (Barnes et al., 2007; R. H. Brown et al., 2005; Elachi et al., 2005; Porco et al., 2005). However, as
304 the best resolution for such orbital data (SAR's ~350 m/pixel) is much coarser than DISR's images
305 (~15-30 m/pixel), only the largest fluvial valleys (including the surrounding valley walls and their
306 relative SAR-shadowing on the riverbed) are supposedly identified, while the individual channels
307 should not (Birch et al., 2017; Burr et al., 2009; Moore & Pappalardo, 2011). Therefore, the local
308 features observed in this work have been interpreted as fluvial valleys and thus termed accordingly.

309

310 The distinctive high σ^0 of the FVU is most probably due to an elevated density of icy rounded
311 pebbles with size larger than RADAR wavelength (> 2.17 cm) (Le Gall et al., 2010). The observed
312 decrease in width and brightness with distance may be due to evaporation and/or infiltration over
313 the SPU (Sup. Figure 2g). Alternatively, the change in appearance may result from selective sorting
314 as the slope drops and the flow is less confined, although it must be considered that there is a slight
315 difference in the look angle upstream to downstream (20° to 25°) (Burr, Drummond, et al., 2013; Le
316 Gall et al., 2010; Maue & Burr, 2018).

317

318 **3.1.8.1 Fluvial Subunits**

319 In some limited areas a differentiation among the FVU has been made. This resulted in two
320 subunits, a Meander Belt one (marked in aquamarine; Figure 1b and Sup. Figure 2h) and a Deltaic
321 one (marked in dark green; Figure 1b and Sup. Figure 2h). Given their direct correlation with the
322 FVU and very limited extent, these units have not been formally defined as constituting separate
323 ones, yet they have been distinguished from the main unit by using a different mapping color. Their
324 definition and significance are described in Section 3.2.1.

325

326 **3.2 Geomorphology, tectonic indicators and topography**

327 Figure 1b represents the geomorphological map of southwestern Xanadu, as a result of this study.
328 The Rough Highlands Unit (RHU) and Dissected Highlands Unit (DHU) (all units are defined and
329 described in Section 3.1) are the prevalent geomorphological units towards the inner portions of the
330 region, N and E, while the Smooth Plains Unit (SPU) dominates towards S and W. To the very W
331 of the mapped area, the Linear Dunes Unit (LDU) is widespread and surrounds a few patches of
332 DHU, Impact Crater Unit (ICU) and Dark Mottled Unit (DMU). Most of the units' boundaries in
333 the mapped area are either gradational or not easily distinguishable. The most abrupt contact is
334 aligned roughly NW-SE (from 20°S; 118°W to 15°S; 128°W) along a sharp linear feature; several

unit boundaries are located along it (Figures 1, 4b). Within the majority of the mapped units, there is a superimposition of fluvial units: Fluvial Valleys Unit (FVU), and relative subunits.

Based on both SARTopo and DTM data, the overall average elevation values of SW Xanadu are between -400 m and 400 m. This study mostly relied on DTM data, as their error range is lower and offer a wide spatial coverage on the area investigated; see Section 2. The topographic profiles shown in Figure 3 clearly expose how topographic peaks are present all over the mapped area, yet the average elevation decreases NW to SE (and W to E). Thus, both SARTopo and DTM data suggest the presence of a topographic gradient along these axes.

In Figure 3, going from A (C) to B (D) along the topographic profiles, a positive elevation gradient is identified, followed by a marked drop mainly corresponding to outcrops of DHU, E of the Shangri-La dune field (from ~10°S; 142°W to ~3°S; 138°W, the Shangri-La dune field is marked as LDU on the geomorphological map, Figure 1b). In central SW Xanadu, which is dominated by fluvial features, the average elevation is lower compared to the previously mentioned areas to the W; the main topographic drops correspond to the widest fluvial valleys (FVU).

To the very E, the topography gradually increases again along what seems a W-dipping tilted block (Figure 3). In this part of the mapped area, a N-S striking linear feature is recognizable (10°S; 110°W), on both SAR images and DTM data (Figure 5). On DTM's 3D visualization (Figure 5c), it looks as a continuous W-dipping plane, tilted at a more or less constant angle of 2-6°. It extends for ~170 km and crosscuts two other similar features (9°S; 108°W and 11°S; 108°W) which strike roughly NW-SE (dip ~200°W) parallel to each other and also to the aforementioned sharp linear feature located around 20°S; 118°W.

In the northern portions of the mapped area (2°S; 127°W) three aligned structures have been encountered (Figure 4c). These are already described in the literature (Mitri et al., 2010; Jani Radebaugh et al., 2016) and were interpreted in such works as long-wavelength folds formed by compressional tectonics (IAU nomenclature: "Mithrim Montes").

The fluvial network (marked as FVU in the geomorphological map, Figure 1b) in central SW Xanadu seems to deviate from an hypothetical draining direction that is driven only by the local NW-SE topographic gradient: i.e. a draining direction that would form a dendritic pattern, see Twidale (2004). This effect is probably due to the imposition of the fluvial network on some pre-existing E-W, SW-NE and NW-SE linear features (Figure 4a), as outlined by the drainage system rose diagram's results (Figure 2a). Red lines point out the portions on the geomorphological map where this effect is most evident; rose diagram's results of such linear features are shown in Figure 2b. Eventually, this leads to a rectangular-type pattern (Twidale, 2004) for the connected reaches of the fluvial network at SW Xanadu.

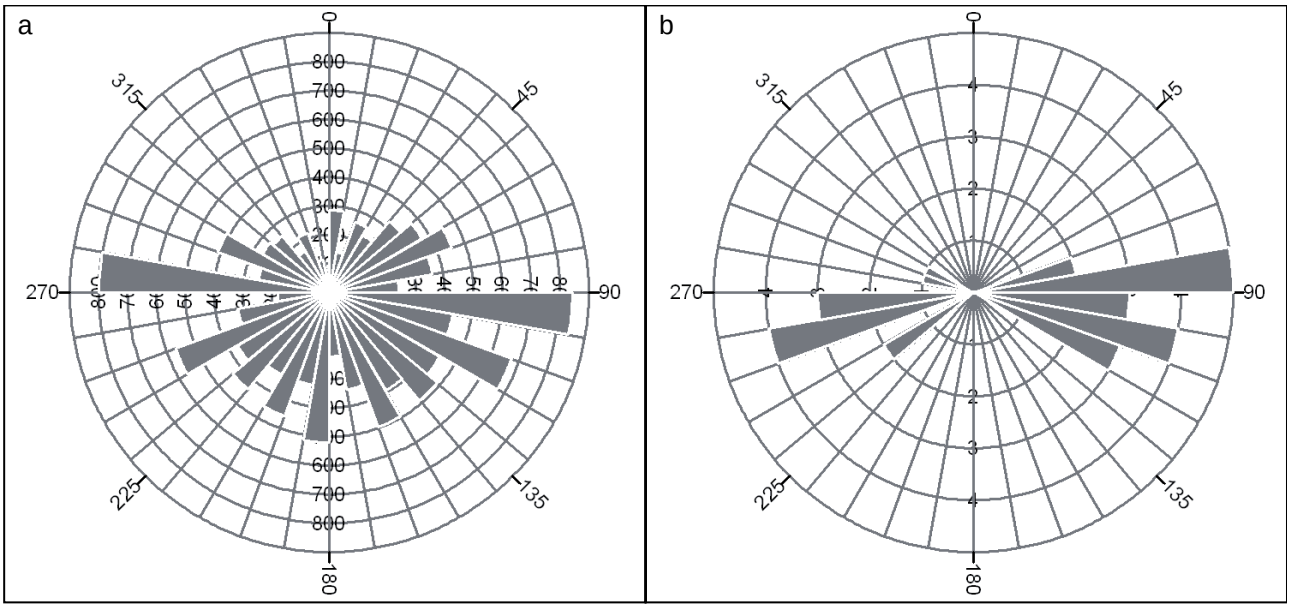

Figure 2. a) Azimuths of the connected reaches of the fluvial network at SW Xanadu displayed in a unidirectional rose diagram (each segment of each valley is analyzed); the cumulative length of the segments is shown divided into 10° bins. The total population of valleys segments is 13,060. A broad, almost uniform, distribution of azimuths exists. The maximum population (843) is located in the 90°-100° bin (roughly E-W), while the mean value is along an E-W trend as well (93°). **b)** Azimuths of 28 linear features, corresponding to abrupt changes in draining direction of the fluvial network at SW Xanadu, displayed in a unidirectional rose diagram; the cumulative length of the

segments is shown divided into 10° bins. The bins with the highest populations are 80°-90°, 100°-110°, 250°-260°.

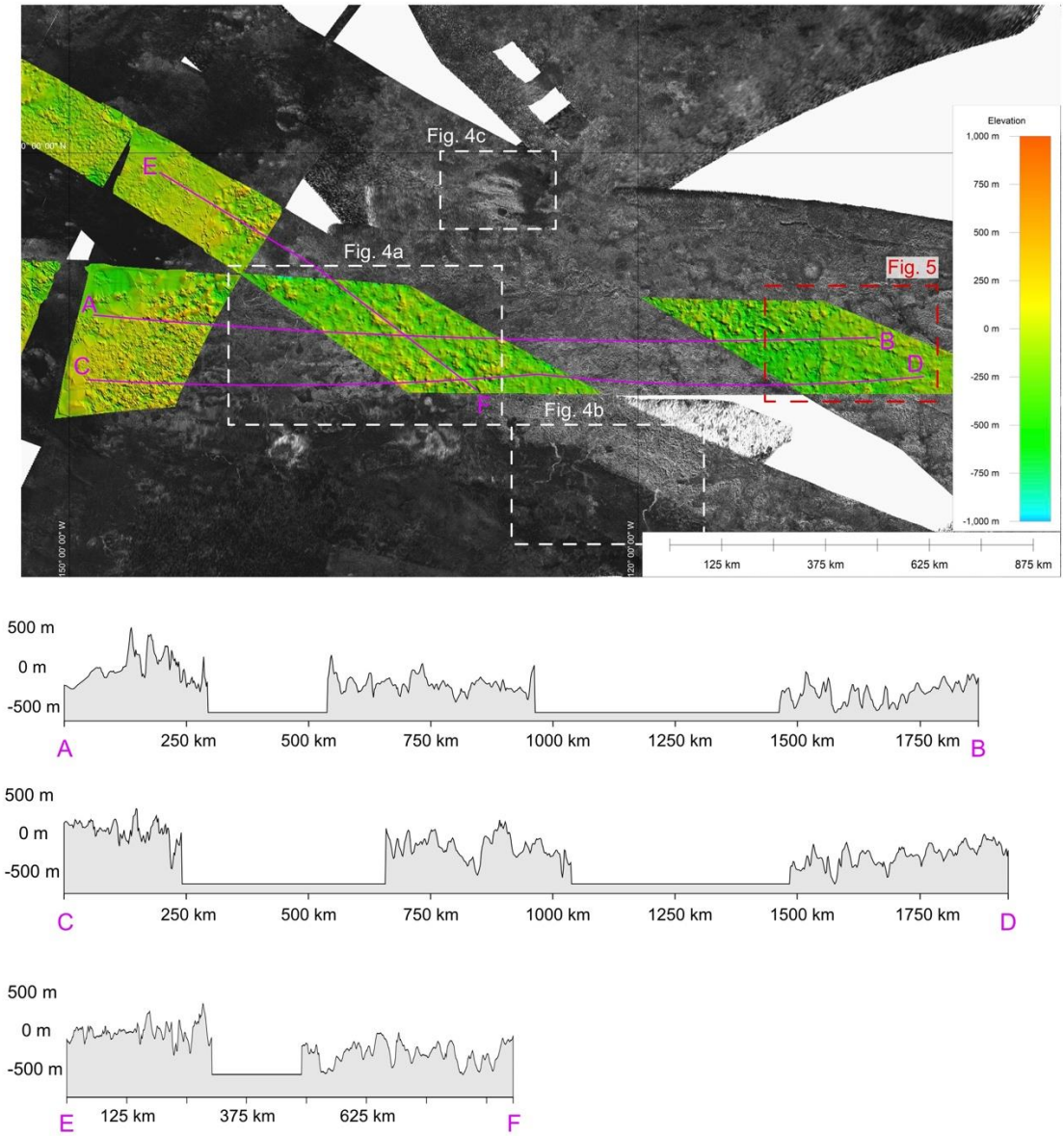

Figure 3. Top) DTMs overlain on SAR mosaic, in 2D visualization. Hillshading is enabled, with a vertical exaggeration factor of 5. The areas shown are SW Xanadu and its surroundings. The white dashed polygons mark the areas shown in Figure 4. The red dashed polygon marks the area shown

in Figure 5. North is up. **Bottom)** Topographic profiles going from A to B and C to D, covering most of the mapped area (Figure 1b) from W to E. The topographic profile going from E to F (NW to SE) crosscuts those going A to B and C to D. The A-B profile is also shown in SW Xanadu's tectonic model in Figure 6.

3.2.1 Interpretation

Southwestern Xanadu is comprised of heavily eroded and rugged terrains to the N and E - corresponding mainly to RHU and DHU - and of smoother and more uniform terrains to the W and S - corresponding mainly to SPU and DMU (Figure 1a-b). An extensive fluvial network is widespread, particularly in the central portions of the examined area (Figure 1a). Fluvial features related to a hydrocarbon cycle on Titan have been identified all over the surface at many different latitude ranges, apart from areas dominated by dune fields (Black et al., 2017; Burr et al., 2009; Burr, Taylor Perron, et al., 2013; Cartwright et al., 2011; A. G. Hayes, 2016; A. G. Hayes et al., 2018; Jaumann et al., 2008; R. M. C. Lopes, Wall, et al., 2019; Maue & Burr, 2018; J. Radebaugh et al., 2016; Reid et al., 2018; Tewelde et al., 2013). Differences in SAR backscatter of different fluvial networks suggest different ages of activity (Le Gall et al., 2010). In SW Xanadu, the general high backscatter of the fluvial valleys probably implies that there is no more liquid runoff and the valleys (FVU) just show remnants of transported material. The presence of liquid would produce a distinctive SAR-darker backscatter as it occurs at the polar rivers, lakes and seas (Birch et al., 2017; A. Hayes et al., 2008; A. G. Hayes, 2016; Mastrogiuseppe et al., 2018; Mitri et al., 2007; Poggiali et al., 2016).

For fluvial networks characterized by many tributaries, as in SW Xanadu, the draining direction is mainly inferred by the direction of tributary confluence (Figures 1, 4a). The presence of downstream depositional sites such as basins/lakes/deltas and upstream sources such as high-roughness terrains, can provide additional evidences to deduce the draining direction (Black et al.,

2017; Burr, Drummond, et al., 2013; Maue & Burr, 2018). In the investigated area, the upstream portions of the drainage basin are located to the N, corresponding to RHU and DHU, whereas SPU and DMU and their surroundings represent the downstream portions of the drainage basin to the S (Figure 1b). In its northern portions this fluvial network is embodied by narrower valleys which tend to continue into wider ones to the S (mainly along the aforementioned sharp linear units' contact, Section 3.2). This is particularly the case towards the SE of the mapped area, around 17°S; 123°W, where several sinuous wide fluvial features are identified: the SAR-brighter ones are thought to contain a higher amount of icy pebbles (Figures 1, 4b). Such material would have been transported and rounded by stream flow, most likely by liquid hydrocarbons during flood events. The pebbles' internal reflections would in turn cause the observed high backscatter, i.e. due to volume scattering (Le Gall et al., 2010). Next to such features some morphologically similar ones, yet SAR-darker, are identified (e.g. 16°S; 123°W, 16°S; 127°W, Figures 1, 4b). These are interpreted as remnants of abandoned rivers, which were active during a previous phase and were darkened either by deposition of fine atmospheric precipitates or by size reduction of the icy pebbles through mechanical weathering (Le Gall et al., 2010). Such interpretation may imply a fluvial system characterized by a good maturity, which is also supported by the large number of tributaries present at the higher portions of the drainage basin. At its lower portions the fluvial network's maturity is suggested by the many existing meandering channels, which were grouped together in the Meander Belt Subunit. Eventually, a distinctive feature that morphologically resembles an Earth's river delta was identified (20°S; 119°W) (Figures 1, 4b) This hypothesis is supported by considering that such feature is located in correspondence of the SAR-darkening portion (i.e., the tip of the fluvial valley, where particles get finer) of one of the most evident, bright fluvial valleys. Only very low-resolution SAR data are available at the tips of nearby fluvial valleys: extending the above interpretation to other features is therefore not possible. Nevertheless, this single feature was classified as part of the Deltaic Subunit. The lack of extensive SAR data coverage is currently leaving any interpretation with some degree of uncertainty.

439 The draining direction during the last active phase of SW Xanadu's fluvial network seems to
440 have been partially driven by a NW-SE local topographic gradient, yet the strong influence of some
441 pre-existing E-W, SW-NE and NW-SE linear features is recorded in the present-day
442 geomorphology (Section 3.2). Analysis of these linear features' azimuths (Figure 2b) and of the
443 abrupt changes in direction of the corresponding fluvial valleys, led to interpret them as evidences
444 of strike-slip faulting in central SW Xanadu (Figure 4a).
445
446 The proposed interpretation of the N-S striking linear feature (10°S; 110°W, Figure 5) is of a W-
447 dipping normal fault plane extending for ~170 km (knowledge limited by DTM's size). This
448 hypothesis is supported by the local topographic trend and by the nearly constant angular values at
449 which the plane is tilted (2-6°). It is not possible to infer the depths reached by the fault with the
450 available data, but, considering its planar extension, it is possible to assume that it constitutes a
451 structure of some relevance, i.e. reaching depths within at least the first few kilometers of the ice
452 shell.
453 The two linear features (9°S; 108°W and 11°S; 108°W, Figure 5), striking roughly NW-SE (dip
454 ~200°W) parallel to each other, are interpreted as normal faults. Due to the different orientation yet
455 similar cinematic (extension) and by considering that these are crosscut by the first one, the last two
456 faults are interpreted as belonging to a previous tectonic phase. The sharp linear feature extending
457 from 20°S; 118°W to 15°S; 128°W strikes parallel to such faults (Figures 1, 4b). Going along-dip
458 on this feature, a distinct change in terrain characteristics is evident (on SAR data); moreover, the
459 local fluvial features show a significant increase in width size crossing it N to S, suggesting the
460 presence of a relevant knick-point (and therefore an important topographic drop). Despite the lack
461 of consistent topographic data (neither SARTopo, nor DTMs) relative to its location, the above
462 considerations led to interpret such feature as a normal fault, in agreement with Radebaugh et al.
463 (2011), This fault would have developed throughout the same tectonic phase of the two mentioned
464 parallel normal faults.

The presence of one or more normal faults is inferred to the western parts of the investigated area: a positive elevation gradient followed by a marked drop is in fact observed E of the Shangri-La dune field (from ~10°S; 142°W to ~3°S; 138°W, Section 3.2 and Figure 3). Such high reliefs might represent a topographic barrier for the Shangri-La dunes, which stop abruptly at this boundary. Distinct fault planes cannot be directly identified, as the surface is intensely reworked and masked by fluvial activity. Nevertheless, the observed, marked elevation drops are limited to a relatively small area, suggesting the occurrence of normal faulting. Without the presence of the numerous fluvial features, we would probably observe similar structures to those previously described to the eastern parts of the investigated area would probably be observed, as the topographical characteristics are analogous.

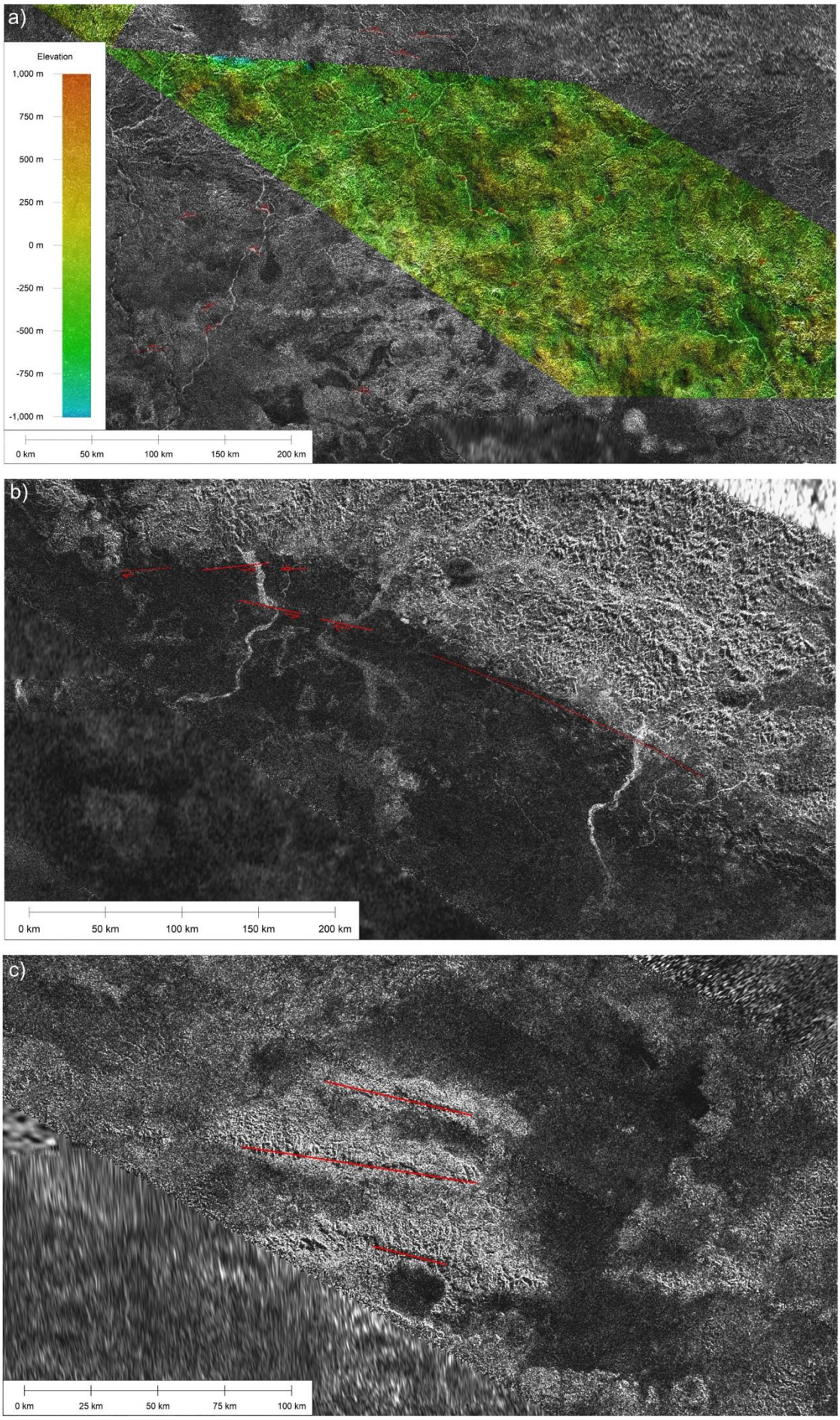
a)
Elevation
1,000 m
750 m
500 m
250 m
0 m
-250 m
-500 m
-750 m
-1,000 m
0 km
50 km
100 km
150 km
200 km
b)
0 km
50 km
100 km
150 km
200 km
c)
0 km
25 km
50 km
75 km
100 km

476

Figure 4. a) Strike-slip faults in central SW Xanadu, shown on a DTM (in overlay mode visualization) over SAR mosaic. Such faults are marked with red lines; the inferred motion direction is indicated. Their azimuthal analysis results are shown in Figure 2b. **b)** SAR mosaic displaying the area around the sharp linear feature (20°S; 118°W to 15°S; 128°W, shown as a fault with a red dashed line) described in the text. **c)** SAR mosaic displaying the area around Mithrim Montes, with their ridges' alignments marked by red lines. North is up in each panel.

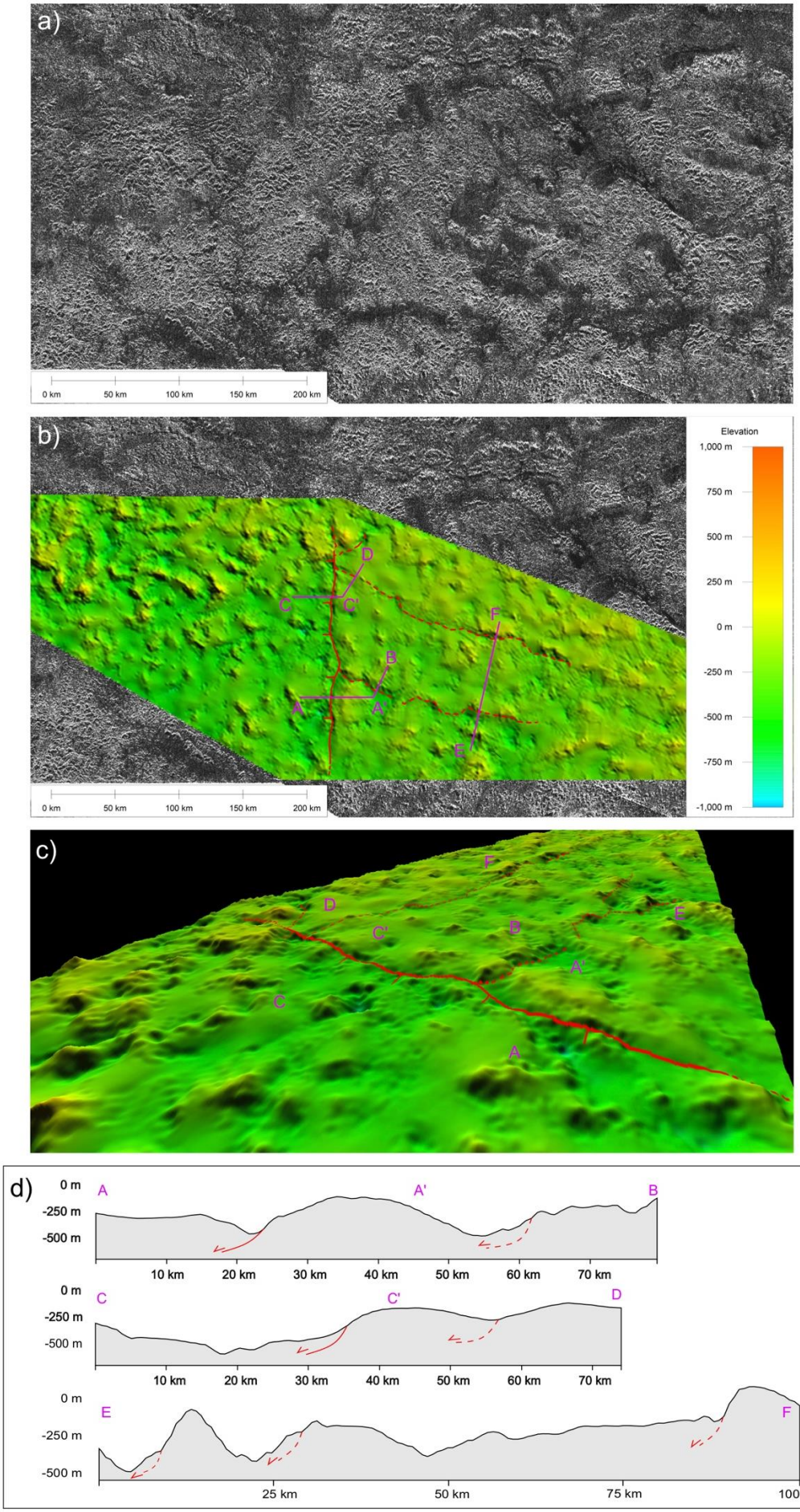
a)
0 km
50 km
100 km
150 km
200 km
b)
Elevation
1,000 m
750 m
500 m
250 m
0 m
-250 m
-500 m
-750 m
-1,000 m
A
A'
B
C
C'
D
E
F
c)
d)
0 m
-250 m
-500 m
10 km
20 km
30 km
40 km
50 km
60 km
70 km
25 km
75 km
100 km

484 **Figure 5. a)** SAR mosaic, displaying the area enclosed by the red dashed polygon in Figure 3. **b)**
485 DTM in 2D visualization overlain on the SAR mosaic shown in panel a. Hill-shading is enabled,
486 with a vertical exaggeration factor of 5. Three distinct fault planes are recognizable and are marked
487 in red. North is up in panels a and b. **c)** DTM in 3D visualization, vertical exaggeration factor of 10.
488 The area and the features shown are the same as in the previous panels; no SAR mosaic in the
489 background. **d)** Topographic profiles, as traced on the map in previous panels. Fault traces are
490 displayed, with their hypothetical inclinations at increasing depth.
491
492 **4. Discussion and conclusions**
493 The hypothesis that Titan has experienced some kind of tectonic activity in the past is strongly
494 supported by both observational data (e.g. eroded mountain chains, Radebaugh et al., 2007; Liu et
495 al., 2016a) and modeling (e.g. compression related long-wavelength folds and fold-and-thrust belts,
496 Mitri et al., 2010). Nevertheless, the intense erosion that affected the mountain ranges and the lack
497 of evidences for recent orogenic features suggest that such tectonic activity has probably ceased and
498 might be long-time quiescent (Langhans et al., 2013; J. Radebaugh et al., 2011).
499 Southwestern Xanadu's characteristics can provide useful insights on Titan's overall tectonic
500 setting. (J. Radebaugh et al., 2011) proposed that in a first tectonic phase, the region underwent
501 crustal thickening via N-S directed regional-scale compression. This phase would have had surface
502 expressions such as E-W oriented parallel mountain ridges (and related valleys) and fold-and-thrust
503 belts. A subsequent extensional event has been invoked to explain present-day Xanadu low
504 elevation, favored by slip along region-bounding faults, resulting in horst-and-graben structures.
505 Langhans et al. (2013) substantially agreed with the evolutionary model proposed by Radebaugh et
506 al. (2011), yet stressing out the important role of rivers as landscape-shaping factor. They studied in
507 detail SW Xanadu fluvial network's azimuths, ending up in assessing an almost uniform azimuthal
508 distribution. An analysis of the relationship between valley network orientations and the present-

509 day topography (Black et al., 2017), further indicates how Titan's mid-latitude and equatorial
510 regions have been stable since the fluvial networks' imposition.
511
512 Our fluvial azimuths' rose diagram results are consistent with those reported by Langhans et al.
513 (2013). Even though we have used a larger data population, we identified a broad distribution of
514 azimuths, yet with a strong maximum roughly aligned E-W (Figure 2a). The outcome of our study
515 is in concordance to previous works, as well (Burr et al., 2009; Burr, Drummond, et al., 2013),
516 which analyzed the main branch of the fluvial network in SW Xanadu and reported that the
517 azimuths have a preferential trend along an E-W orientation. The authors proposed that such
518 orientations form a rectangular-type drainage pattern developed under the influence of tectonic
519 control, with tributaries' azimuths that indicate an E-W tectonic fabric. They considered (Burr et al.,
520 2009) that the regional slope was southward at the time of fluvial network's onset, as indicated by
521 the overall network elongation and the fluvial links converging in a southerly direction. Burr et al.
522 (2013a) have inferred that the tectonic style responsible for generating such rectangular-type
523 drainage pattern was likely extensional, by analogy with terrestrial examples. They observed that
524 the fluvial network has links oriented in a small number of preferred directions, instead in the case
525 of branching (or dendritic) networks the links' orientations would be primarily controlled by the
526 slope direction. The results of the present analysis are in agreement with the above studies, as the
527 rectangularity of the drainage pattern supports the hypothesis of pre-existing tectonic control on SW
528 Xanadu's fluvial network (see also Twidale, 2004), yet we propose a variant interpretation for the
529 involved tectonic style as it is described below.
530
531 Xanadu's horst-and graben model (J. Radebaugh et al., 2011) is considered to generally explain
532 the large-scale evolution of this region. In the smaller-scale area we have analyzed, southwestern
533 Xanadu, the local morphotectonic evidences could possibly be traced back to the proposed sequence
534 of events (compression and subsequent extension). On the other hand, the extensive application of

qualitative analysis on previously unavailable DTMs, has allowed us to interpret such morphotectonic features as originating from a more specific sequence of events characterizing SW Xanadu's evolution:

1) Ancient extensional phase along NW-SE faults.
   Its expressions are:

   - Two NW-SE striking normal faults located around 9°S; 108°W and 11°S; 108°W (Figure 5);

   - One NW-SE striking normal fault located around 20°S; 118°W (Figure 4b);

Each of these structures are parallel to each other and are dipping ~200°W (see Section 3.2.1 for the interpretation as normal faults). This phase's surficial expressions have probably been wiped out, for the most part, by the subsequent tectonic phase and the intense fluvial activity. Indeed, we could identify its expressions mainly to the easternmost parts of SW Xanadu, where there are very few fluvial features compared to its central parts (Figure 1a).

2) More recent tectonic phase driven by large-scale strike-slip faulting (trans-tensional phase).
   Its expressions are:

   - One N-S striking normal fault located at 10°S; 110°W (Figure 5), crosscutting both the first two normal faults of the previous tectonic phase, which confirms its younger age;

   - Some N-S striking normal faults (inferred), located in an area around ~10°S; 142°W to ~3°S; 138°W (Figure 3). Distinct fault planes cannot be directly identified, as the surface

is intensely reworked and masked by fluvial activity. Nevertheless, the observed marked elevation drops are limited to a relatively small area, suggesting the occurrence of normal faulting;

- Three aligned structures (Mithrim Montes) located around 2°S; 127°W (Figure 4c). These are interpreted in literature (Mitri et al., 2010; Radebaugh et al., 2016) as long-wavelength folds formed by compressional tectonics. In absence of additional topographic data (DTMs) on the relevant location, we reckon these structures as being compression related;

- Several E-W, NE-SW and NW-SE strike-slip faults, distributed all over central SW Xanadu (Figure 4a). The local fluvial network imposed on these pre-existing features, as evidenced by the many abrupt changes in the fluvial valleys' directions, resulting in a rectangular-type drainage pattern.

All the surficial expressions of the second tectonic phase are shown in a conceptual model in Figure 6.

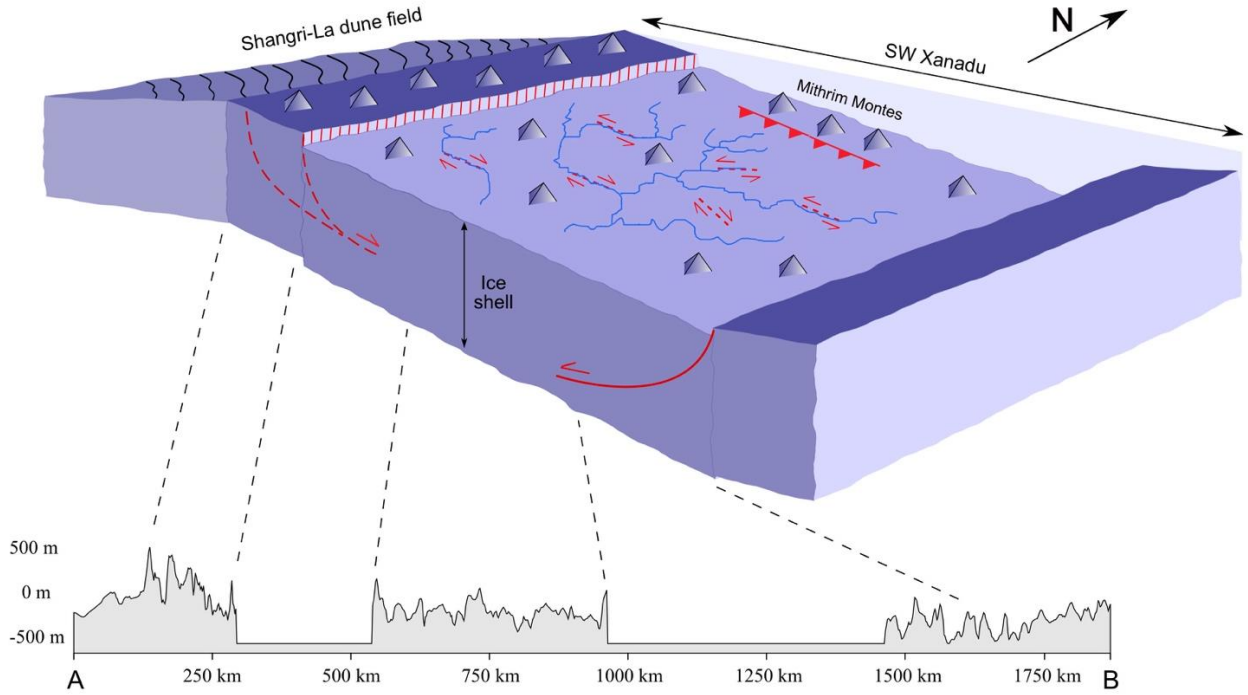

582

583

584 **Figure 6. Top)** Sketched representation of the tectonic setting at southwestern Xanadu. To the W,
585 SW Xanadu is bordered by the Shangri-La dune field. To the N, some compressional structures
586 were identified, which were already known in literature as "Mithrim Montes". **Bottom)**
587 Corresponding topographic profile based on data of three different DTMs (vertical error range: ±
588 100 m), with its location on Titan's SAR mosaic as shown in Figure 4. The sudden breaks of the
589 profile are due to non-available data in the relevant locations. Central SW Xanadu is on average
590 topographically depressed relatively to its surroundings. This is especially noticeable in the case of
591 SW Xanadu's westernmost part, compared to the Shangri-La dune field to the W. This marked
592 elevation drop is interpreted as being due to normal faulting, which is not directly observed but
593 appears evident from topographic profiles. The high reliefs in the western part of SW Xanadu might
594 as well represent a topographic barrier for Shangri-La dunes, which stop abruptly at this boundary.
595 To the E of central SW Xanadu, the identification of a continuous, W-dipping plane, tilted at a more
596 or less constant angle (Figure 5) led to interpret it as a large-scale tectonic structure, namely a
597 normal fault. Overall, this tectonic setting results in a horst-and-graben or half-graben structure.

598 Central SW Xanadu represents the graben, characterized by a fluvial network imposing on pre-
599 existing linear features, which are interpreted as strike-slip faults.
600
601
602 The theoretical structural model proposed (Figure 7) combines all the surficial expressions of the
603 aforementioned second tectonic phase (considered as being the last active one in this area).
604 Generally, in a trans-tensional setting the master fault zone is a large-scale transcurrent structure,
605 whose main stresses can be divided into their compressional and extensional components (Fossen et
606 al., 1994; Petit, 1987). In the case of SW Xanadu, the extensional component should be more
607 intense as it generates extensive and well-developed structures compared to those related to
608 compressional stresses. Such stress field generates a tectonic basin in its central portions,
609 specifically termed *pull-apart* basin (Mann et al., 1983). The strike-slip faulting characterizing
610 central SW Xanadu would have been formed in this setting as well, as synthetic and antithetic
611 Riedel structures to the transcurrent master fault zone (Fossen et al., 1994; Petit, 1987). It must be
612 noticed that we did not directly observe said master fault zone, as it should be a regional-scale
613 structure located outside of the mapped area, yet its direction (roughly SW-NE) was inferred by
614 analyzing the angular relationships of SW Xanadu's aforementioned structures, as identified
615 through geomorphological and topographical analysis. We could not locate one of the hypothesized
616 compressional structures in the structural model, which predicts symmetrical thrust faulting on both
617 sides of the strain ellipse. Evidences of thrust faulting were in fact identified just to the N of the
618 mapped area (Mithrim Montes; around 2°S; 127°W) while not to the S. Anyhow, this is probably
619 due to topographic data absence and to poor resolution of SAR images (where present) in the
620 southern parts of the mapped area.
621 Such trans-tensional structural model is in agreement with Titan's global radial contraction
622 through volume decrease predicted in Mitri et al. (2010), considering SW Xanadu's master
623 transcurrent fault zone as being related to other potential structures with a similar cinematic on a

global scale. Therefore, if there is radial contraction on Titan, intensity differences among components should be present within the stress field. In this setting, large-scale transcurrent faulting would occur.

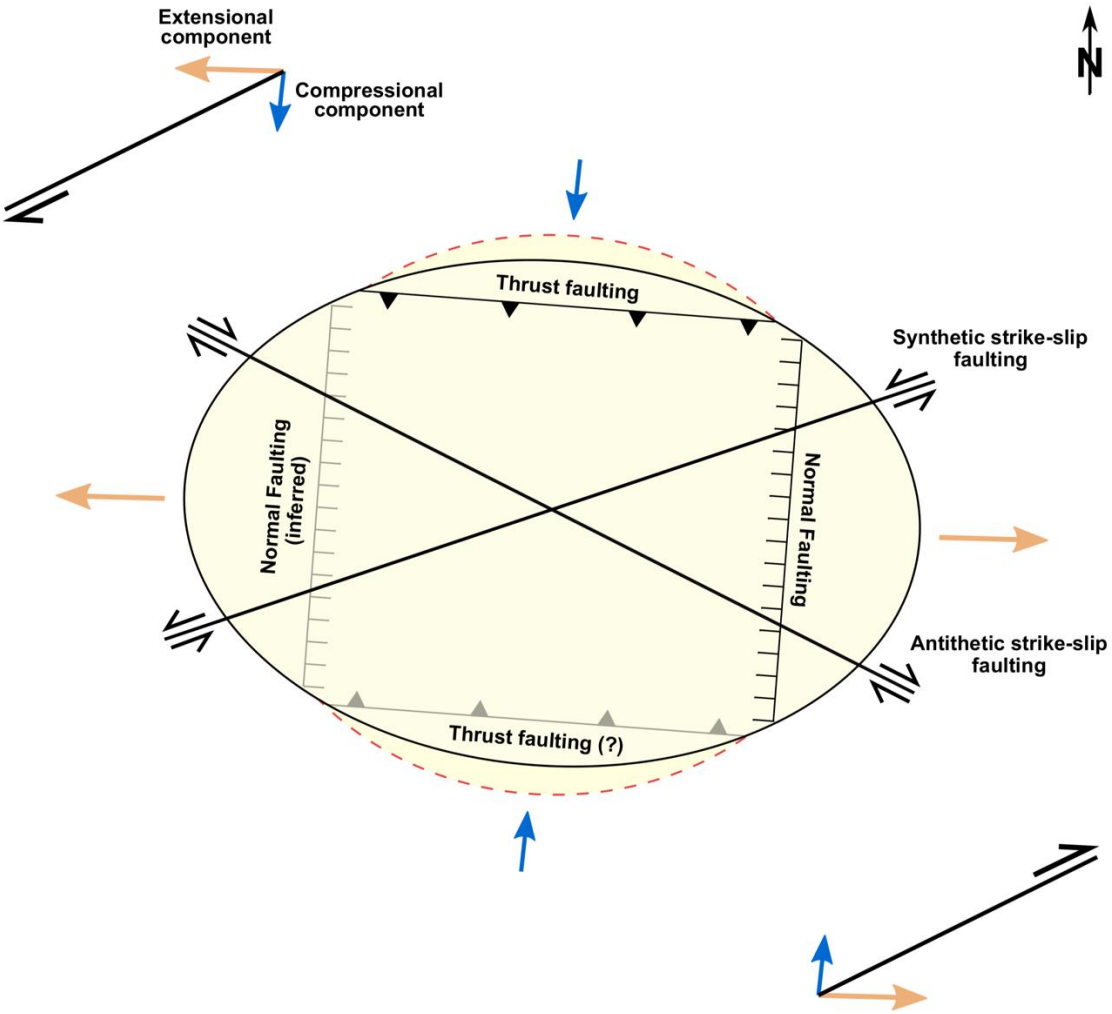

Figure 7. SW Xanadu's theoretical structural model at a regional scale. Strain ellipses are displayed in light yellow. Riedel structures, formed following trans-tensional kinematic criteria driven by large-scale transcurrent faulting, are shown in black. All of SW Xanadu's features described in the text are located within the strain ellipses.

We conclude that central SW Xanadu is a depression formed by trans-tensional tectonic activity, i.e. it is a pull-apart basin, bordered to the W and E by large-scale normal faulting and to the N and (probably) S by thrust faulting of lesser relevance. Such pull-apart basin is characterized by strike-slip faulting within it, on which a now inactive fluvial network subsequently imposed. This model may explain how SW Xanadu has lower elevations compared to its surroundings, while still being a topographically rugged region.

Acknowledgments

PM was supported by Latium Region's Study and Knowledge Promotion (DiSCo) Programme 2018- 19, European Social Fund 2014-20. All the data sets used in this manuscript can be accessed from the PDS Cartography and Imaging Science Node (https://pds-imaging.jpl.nasa.gov/volumes/radar.html).

References

Aharonson, O., Hayes, A. G., Hayne, P. O., Lopes, R. M., Lucas, A., & Perron, J. T. (2013). Titan. In *Titan: Interior, Surface, Atmosphere, and Space Environment* (pp. 63–101). Cambridge Press University. https://doi.org/10.1017/CBO9780511667398

Barnes, J. W., Radebaugh, J., Brown, R. H., Wall, S., Soderblom, L., Lunine, J., et al. (2007). Near-infrared spectral mapping of Titan's mountains and channels. *Journal of Geophysical Research: Planets*, *112*(11). https://doi.org/10.1029/2007JE002932

Birch, S. P. D., Hayes, A. G., Howard, A. D., Moore, J. M., & Radebaugh, J. (2016). Alluvial Fan Morphology, distribution and formation on Titan. *Icarus*, *270*, 238–247. https://doi.org/10.1016/j.icarus.2016.02.013

Birch, S. P. D., Hayes, A. G., Dietrich, W. E., Howard, A. D., Bristow, C. S., Malaska, M. J., et al. (2017). Geomorphologic mapping of titan's polar terrains: Constraining surface processes and landscape evolution. *Icarus*, *282*, 214–236. https://doi.org/10.1016/j.icarus.2016.08.003

Black, B. A., Perron, J. T., Burr, D. M., & Drummond, S. A. (2012). Estimating erosional exhumation on Titan from drainage network morphology. *Journal of Geophysical Research: Planets*, *117*(8), 1–17. https://doi.org/10.1029/2012JE004085

Black, B. A., Perron, J. T., Hemingway, D., Bailey, E., Nimmo, F., & Zebker, H. (2017). Planetary topography: Global drainage patterns and the origins of topographic relief on Earth, Mars, and Titan. *Science*, *356*(6339), 727–731. https://doi.org/10.1126/science.aag0171

Bottke, W. F., & Norman, M. D. (2017). The Late Heavy Bombardment. *Annual Review of Earth and Planetary Sciences*, *45*(1), 619–647. https://doi.org/10.1146/annurev-earth-063016-020131

Brown, R. H., Baines, K. H., Bellucci, G., Bibring, J. P., Buratti, B. J., Capaccioni, F., et al. (2005). The Cassini visual and infrared mapping spectrometer (VIMS) investigation. *Space Science Reviews*, *115*(1–4), 111–168. https://doi.org/10.1007/s11214-004-1453-x

Brown, Robert H., Barnes, J. W., & Melosh, H. J. (2011). On Titan's Xanadu region. *Icarus*, *214*(2), 556–560. https://doi.org/10.1016/j.icarus.2011.03.018

Burr, D. M., Jacobsen, R. E., Roth, D. L., Phillips, C. B., Mitchell, K. L., & Viola, D. (2009). Fluvial network analysis on Titan: Evidence for subsurface structures and west-to-east wind flow, southwestern Xanadu. *Geophysical Research Letters*, *36*(22), 1–5. https://doi.org/10.1029/2009GL040909

Burr, D. M., Taylor Perron, J., Lamb, M. P., Irwin, R. P., Collins, G. C., Howard, A. D., et al. (2013). Fluvial features on Titan: Insights from morphology and modeling. *Bulletin of the Geological Society of America*, *125*(3–4), 299–321. https://doi.org/10.1130/B30612.1

Burr, D. M., Drummond, S. A., Cartwright, R., Black, B. A., & Perron, J. T. (2013). Morphology of fluvial networks on Titan: Evidence for structural control. *Icarus*, *226*(1), 742–759. https://doi.org/10.1016/j.icarus.2013.06.016

Cartwright, R., Clayton, J. A., & Kirk, R. L. (2011). Channel morphometry, sediment transport, and implications for tectonic activity and surficial ages of Titan basins. *Icarus*, *214*(2), 561–570.

https://doi.org/10.1016/j.icarus.2011.03.011

Cook-Hallett, C., Barnes, J. W., Kattenhorn, S. A., Hurford, T., Radebaugh, J., Stiles, B., & Beuthe, M. (2015). Global contraction/expansion and polar lithospheric thinning on Titan from patterns of tectonism. *Journal of Geophysical Research: Planets*, *120*(6), 1220–1236. https://doi.org/10.1002/2014JE004645

Corlies, P., Hayes, A. G., Birch, S. P. D., Lorenz, R., Stiles, B. W., Kirk, R., et al. (2017). Titan's Topography and Shape at the End of the Cassini Mission. *Geophysical Research Letters*, *44*(23), 11, 754-11, 761. https://doi.org/10.1002/2017GL075518

Coustenis, A., Tokano, T., Burger, M. H., Cassidy, T. A., Lopes, R. M., Lorenz, R. D., et al. (2010). Atmospheric/exospheric characteristics of icy satellites. *Space Science Reviews*, *153*(1–4), 155–184. https://doi.org/10.1007/s11214-009-9615-5

Coustenis, Athena. (2005). Formation and evolution of Titan's atmosphere. *Space Science Reviews*, *116*(1–2), 171–184. https://doi.org/10.1007/s11214-005-1954-2

Dalton, J. B., Cruikshank, D. P., Stephan, K., McCord, T. B., Coustenis, A., Carlson, R. W., & Coradini, A. (2010). Chemical composition of icy satellite surfaces. *Space Science Reviews*, *153(*1-4), 113-154. https://doi.org/10.1007/s11214-010-9665-8

Elachi, C., Allison, M. D., Borgarelli, L., Encrenaz, P., Im, E., Janssen, M. A., et al. (2005). Radar: The Cassini Titan RADAR mapper. *Space Science Reviews*, *115*(1–4), 71–110. https://doi.org/10.1007/s11214-004-1438-9

Elachi, C., Wall, S., Janssen, M., Stofan, E., Lopes, R., Kirk, R., et al. (2006). Titan Radar Mapper observations from Cassini's T3 fly-by. *Nature*, *441*(7094), 709–713. https://doi.org/10.1038/nature04786

Ford, J. P., Weitz, J. J. P. C. M., Farr, T. G., Senske, D. A., Stofan, E. R., Michaels, G., & Parker, T. J. (1993). *Guide to Magellan Image Interpretation*. *Jet Propulsion Laboratory, Cap. Radar Interactions With Geologic Surfaces*. http://web.archive.org/web/19990420173536/http://pds.jpl.nasa.gov/mgddf/guide.htm

714 Fossen, H., Tikoff, B., & Teyssier, C. (1994). Strain modeling of transpressional and transtensional
715 deformation. *Norsk Geologisk Tidsskrift*, *74*(3), 134–145.
716 Le Gall, A., Janssen, M. A., Paillou, P., Lorenz, R. D., & Wall, S. D. (2010). Radar-bright channels
717 on Titan. *Icarus*, *207*(2), 948–958. https://doi.org/10.1016/j.icarus.2009.12.027
718 Hayes, A., Aharonson, O., Callahan, P., Elachi, C., Gim, Y., Kirk, R., et al. (2008). Hydrocarbon
719 lakes on Titan: Distribution and interaction with a porous regolith. *Geophysical Research*
720 *Letters*, *35*(9), 1–6. https://doi.org/10.1029/2008GL033409
721 Hayes, A. G. (2016). The Lakes and Seas of Titan. *Annual Review of Earth and Planetary Sciences*,
722 *44*(1), 57–83. https://doi.org/10.1146/annurev-earth-060115-012247
723 Hayes, A. G., Lorenz, R. D., & Lunine, J. I. (2018). A post-Cassini view of Titan's methane-based
724 hydrologic cycle. *Nature Geoscience*, *11*(5), 306–313. https://doi.org/10.1038/s41561-018-
725 0103-y
726 Iess, L., Jacobson, R. A., Ducci, M., Stevenson, D. J., Lunine, J. I., Armstrong, J. W., et al. (2012).
727 The tides of Titan. *Science*, *337*(6093), 457–459. https://doi.org/10.1126/science.1219631
728 Jaumann, R., Brown, R. H., Stephan, K., Barnes, J. W., Soderblom, L. A., Sotin, C., et al. (2008).
729 Fluvial erosion and post-erosional processes on Titan. *Icarus*, *197*(2), 526–538.
730 https://doi.org/10.1016/j.icarus.2008.06.002
731 Kirk, R. L., Howington-Kraus, E., Redding, B., Callahan, P. S., Hayes, a. G., Legall, a., et al.
732 (2012). Topographic Mapping of Titan: Latest Results. *Lunar and Planetary Science*
733 *Conference*, *43*, 2759. http://adsabs.harvard.edu/abs/2012LPI....43.2759K
734 Langhans, M., Lunine, J. I., & Mitri, G. (2013). Titan's Xanadu region: Geomorphology and
735 formation scenario. *Icarus*, *223*(2), 796–803. https://doi.org/10.1016/j.icarus.2013.01.016
736 Liu, Z. Y. C., Radebaugh, J., Harris, R. A., Christiansen, E. H., & Rupper, S. (2016). Role of fluids
737 in the tectonic evolution of Titan. *Icarus*, *270*, 2–13.
738 https://doi.org/10.1016/j.icarus.2016.02.016
739 Liu, Z. Y. C., Radebaugh, J., Harris, R. A., Christiansen, E. H., Neish, C. D., Kirk, R. L., & Lorenz,

R. D. (2016). The tectonics of Titan: Global structural mapping from Cassini RADAR. *Icarus*, *270*, 14–29. https://doi.org/10.1016/j.icarus.2015.11.021

Lopes, R. M. C., Malaska, M. J., Schoenfeld, A. M., Solomonidou, A., Birch, S. P. D., Florence, M., et al. (2019). A global geomorphologic map of Saturn's moon Titan. *Nature Astronomy*, 1–6. https://doi.org/10.1038/s41550-019-0917-6

Lopes, R. M. C., Wall, S. D., Elachi, C., Birch, S. P. D., Corlies, P., Coustenis, A., et al. (2019). Titan as Revealed by the Cassini Radar. *Space Science Reviews*, *215*(4), 33. https://doi.org/10.1007/s11214-019-0598-6

Lopes, R. M. C., Stofan, E. R., Peckyno, R., Radebaugh, J., Mitchell, K. L., Mitri, G., et al. (2010). Distribution and interplay of geologic processes on Titan from Cassini radar data. *Icarus*, *205*(2), 540–558. https://doi.org/10.1016/j.icarus.2009.08.010

Lopes, Rosaly M.C., Malaska, M. J., Solomonidou, A., Le Gall, A., Janssen, M. A., Neish, C. D., et al. (2016). Nature, distribution, and origin of Titan's Undifferentiated Plains. *Icarus*, *270*, 162–182. https://doi.org/10.1016/j.icarus.2015.11.034

Lorenz, R. D., Lopes, R. M., Paganelli, F., Lunine, J. I., Kirk, R. L., Mitchell, K. L., et al. (2008). Fluvial channels on Titan: Initial Cassini RADAR observations. *Planetary and Space Science*, *56*(8), 1132–1144. https://doi.org/10.1016/j.pss.2008.02.009

Lorenz, R. D., Stiles, B. W., Aharonson, O., Lucas, A., Hayes, A. G., Kirk, R. L., et al. (2013). A global topographic map of Titan. *Icarus*, *225*(1), 367–377. https://doi.org/10.1016/j.icarus.2013.04.002

Lunine, J. I. (2017). Ocean worlds exploration. *Acta Astronautica*, *131*, 123–130. https://doi.org/10.1016/j.actaastro.2016.11.017

Malaska, M. J., Lopes, R. M. C., Williams, D. A., Neish, C. D., Solomonidou, A., Soderblom, J. M., et al. (2016). Geomorphological map of the Afekan Crater region, Titan: Terrain relationships in the equatorial and mid-latitude regions. *Icarus*, *270*, 130–161. https://doi.org/10.1016/j.icarus.2016.02.021

766 Malaska, M. J., Lopes, R. M., Hayes, A. G., Radebaugh, J., Lorenz, R. D., & Turtle, E. P. (2016).
767 Material transport map of Titan: The fate of dunes. *Icarus*, *270*, 183–196.
768 https://doi.org/10.1016/j.icarus.2015.09.029
769 Mann, P., Hempton, M. R., Burke, K., & Bradley, D. C. (1983). Development of Pull-Apart Basins.
770 *The Journal of Geology*, *91*(5), 529–554.
771 Mastrogiuseppe, M., Poggiali, V., Seu, R., Martufi, R., & Notarnicola, C. (2014). Titan dune
772 heights retrieval by using Cassini Radar Altimeter. *Icarus*, *230*, 191–197.
773 https://doi.org/10.1016/j.icarus.2013.09.028
774 Mastrogiuseppe, M., Poggiali, V., Hayes, A. G., Lunine, J. I., Seu, R., Di Achille, G., & Lorenz, R.
775 D. (2018). Cassini radar observation of Punga Mare and environs: Bathymetry and
776 composition. *Earth and Planetary Science Letters*, *496*, 89–95.
777 https://doi.org/10.1016/j.epsl.2018.05.033
778 Mastrogiuseppe, M., Poggiali, V., Hayes, A. G., Lunine, J. I., Seu, R., Mitri, G., & Lorenz, R. D.
779 (2019). Deep and methane-rich lakes on Titan. *Nature Astronomy*, *3*, 535-542.
780 https://doi.org/10.1038/s41550-019-0714-2
781 Maue, A., & Burr, D. (2018). Updating the Global Map of Titan Fluvial Features and
782 Investigating Downstream Radar Brightness Trends. *Planetary Geologic Mappers Meeting*,
783 *2018* (2066), 7–8.
784 Mitri, G., Showman, A. P., Lunine, J. I., & Lorenz, R. D. (2007). Hydrocarbon lakes on Titan.
785 *Icarus*, *186*(2), 385–394. https://doi.org/10.1016/j.icarus.2006.09.004
786 Mitri, G., Bland, M. T., Showman, A. P., Radebaugh, J., Stiles, B., Lopes, R. M. C., et al. (2010).
787 Mountains on Titan: Modeling and observations. *Journal of Geophysical Research: Planets*,
788 *115*(10), 1–15. https://doi.org/10.1029/2010JE003592
789 Mitri, G., Meriggiola, R., Hayes, A., Lefevre, A., Tobie, G., Genova, A., et al. (2014). Shape,
790 topography, gravity anomalies and tidal deformation of Titan. *Icarus*, *236*, 169–177.
791 https://doi.org/10.1016/j.icarus.2014.03.018

792 Mitri, G., Lunine, J. I., Mastrogiuseppe, M., & Poggiali, V. (2019). Possible explosion crater origin
793 of small lake basins with raised rims on Titan. *Nature Geoscience, 12,* 791-796.
794 https://doi.org/10.1038/s41561-019-0429-0
795 Moore, J. M., & Pappalardo, R. T. (2011). Titan: An exogenic world? *Icarus*, *212*(2), 790–806.
796 https://doi.org/10.1016/j.icarus.2011.01.019
797 Moore, J. M., Howard, A. D., Morgan, A. M., Howard, A. D., & Morgan, A. M. (2014). Landscape
798 of Titan as witness to its climate evolution, *119* (9), 2066-2077.
799 https://doi.org/10.1002/2014JE004608.Received
800 Neish, C. D., Molaro, J. L., Lora, J. M., Howard, A. D., Kirk, R. L., Schenk, P., et al. (2016).
801 Fluvial erosion as a mechanism for crater modification on Titan. *Icarus, 270,* 114–129.
802 https://doi.org/10.1016/j.icarus.2015.07.022
803 Nimmo, F. (2018). Icy satellites: Interior structure, dynamics and evolution. In *Oxford Research*
804 *Encyclopedia of Planetary Sciences*.
805 https://websites.pmc.ucsc.edu/~fnimmo/website/Oxford_article_revised.pdf
806 Petit, J. P. (1987). Criteria for the sense of movement on fault surfaces in brittle rocks. *Journal of*
807 *Structural Geology*, *9*(5–6), 597–608. https://doi.org/10.1016/0191-8141(87)90145-3
808 Poggiali, V., Mastrogiuseppe, M., Birch, S. P. D., Lorenz, R., Seu, R., Grima, C., et al. (2016).
809 Liquid-filled canyons on Titan. *Geophysical Research Letters*, *43*(15), 7887–7894.
810 https://doi.org/10.1002/2016gl069679
811 Porco, C. C., West, R. A., Squyres, S., McEwen, A., Thomas, P., Murray, C. D., et al. (2005).
812 Cassini imaging science: Instrument characteristics and anticipated scientific investigations at
813 Saturn. *Space Science Reviews*, *115*(1–4), 363–497. https://doi.org/10.1007/s11214-004-1456-
814 7
815 Radebaugh, J., Lorenz, R. D., Lunine, J. I., Wall, S. D., Boubin, G., Reffet, E., et al. (2008). Dunes
816 on Titan observed by Cassini Radar. *Icarus*, *194*(2), 690–703.
817 https://doi.org/10.1016/j.icarus.2007.10.015

Radebaugh, J., Lorenz, R. D., Wall, S. D., Kirk, R. L., Wood, C. A., Lunine, J. I., et al. (2011). Regional geomorphology and history of Titan's Xanadu province. *Icarus*, *211*(1), 672–685. https://doi.org/10.1016/j.icarus.2010.07.022

Radebaugh, J., Lorenz, R. D., Ventra, D., Farr, T., Kirk, R., Lunine, J., et al. (2016). Alluvial and fluvial fans on Saturn's moon Titan reveal processes, materials and regional geology. *Journal of the Geological Society*. https://doi.org/10.1144/SP440.6

Radebaugh, Jani, Lopes, R. M. C., Lunine, J. I., Kirk, R. L., Wall, S. D., Radebaugh, J., et al. (2007). Mountains on Titan observed by Cassini Radar. *Icarus*, *192*(1), 77–91. https://doi.org/10.1016/j.icarus.2007.06.020

Radebaugh, Jani, Lorenz, R. D., Liu, Z. Y.-C., & Kirk, R. L. (2016). The highest point on Titan. *Lunar and Planetary Science Conference XLVII*, *84602*, 46–47. https://doi.org/10.1038/ngeo2474.

Reid, R. P., Kozdon, R., Orland, I. J., Valley, J. W., Noah, J., Casaburi, G., & Foster, J. S. (2018). Fluvial geomorphology on Earth-like planetary surfaces: A review. *17*(5), 413–430. https://doi.org/10.1089/ast.2016.1563.A

Solomonidou, A., Bampasidis, G., Hirtzig, M., Coustenis, A., Kyriakopoulos, K., St. Seymour, K., et al. (2013). Morphotectonic features on Titan and their possible origin. *Planetary and Space Science*, *77*, 104–117. https://doi.org/10.1016/j.pss.2012.05.003

Stern, R. J., Gerya, T., & Tackley, P. J. (2018). Stagnant lid tectonics: Perspectives from silicate planets, dwarf planets, large moons, and large asteroids. *Geoscience Frontiers*, *9*(1), 103–119. https://doi.org/10.1016/j.gsf.2017.06.004

Stiles, B. W., Hensley, S., Gim, Y., Bates, D. M., Kirk, R. L., Hayes, A., et al. (2009). Determining Titan surface topography from Cassini SAR data. *Icarus*, *202*(2), 584–598. https://doi.org/10.1016/j.icarus.2009.03.032

Stofan, E. R., Lunine, J. I., Lopes, R., Paganelli, F., Lorenz, R. D., Wood, C. A., et al. (2006). Mapping of Titan: Results from the first Titan radar passes. *Icarus*, *185*(2), 443–456.

844 https://doi.org/10.1016/j.icarus.2006.07.015
845 Stofan, E. R., Elachi, C., Lunine, J. I., Lorenz, R. D., Stiles, B., Mitchell, K. L., et al. (2007). The
846 lakes of Titan. *Nature*, *445*(7123), 61–64. https://doi.org/10.1038/nature05438
847 Stofan, Ellen R, Wall, S. D., Stiles, B. W., Kirk, R. L., West, R. D., & Callahan, P. S. (2008).
848 Cassini Radar Users Guide. *JPL User Guide*.
849 Tewelde, Y., Perron, J. T., Ford, P., Miller, S., & Black, B. (2013). Estimates of fluvial erosion on
850 Titan from sinuosity of lake shorelines. *Journal of Geophysical Research: Planets*, *118*(10),
851 2198–2212. https://doi.org/10.1002/jgre.20153
852 Tobie, G., Lunine, J. I., & Sotin, C. (2006). Episodic outgassing as the origin of atmospheric
853 methane on Titan. *Nature*, *440*(7080), 61–64. https://doi.org/10.1038/nature04497
854 Tomasko, M. G., Archinal, B., Becker, T., Bézard, B., Bushroe, M., Combes, M., et al. (2005).
855 Rain, winds and haze during the Huygens probe's descent to Titan's surface. *Nature*,
856 *438*(7069), 765–778. https://doi.org/10.1038/nature04126
857 Twidale, C. R. (2004). River patterns and their meaning. *Earth-Science Reviews*, *67*(3–4), 159–218.
858 https://doi.org/10.1016/j.earscirev.2004.03.001
859 Williams, D. A., Radebaugh, J., Lopes, R. M. C., & Stofan, E. (2011). Geomorphologic mapping of
860 the Menrva region of Titan using Cassini RADAR data. *Icarus*, 212(2), 744-750
861 https://doi.org/10.1016/j.icarus.2011.01.014
862 Witek, P. P., & Czechowski, L. (2015). Dynamical modelling of river deltas on Titan and Earth.
863 *Planetary and Space Science*, *105*, 65–79. https://doi.org/10.1016/j.pss.2014.11.005
864 Wood, C. A., Lorenz, R., Kirk, R., Lopes, R., Mitchell, K., & Stofan, E. (2010). Impact craters on
865 Titan. *Icarus*, *206*(1), 334–344. https://doi.org/10.1016/j.icarus.2009.08.021
866 Zebker, H. A., Stiles, B., Hensley, S., Lorenz, R., Kirk, R. L., & Lunine, J. (2009). Size and Shape
867 of Titan. *Science*, *324*, 921–923. https://doi.org/10.1126/science.1168905
868